Perez, H., Pidcock, M. and Sebu, C. (2017) 'A three-dimensional image reconstruction algorithm for electrical impedance tomography using planar electrode arrays', *Inverse Problems in Science and Engineering*, 25 (4), pp. 471-491.

DOI: https://doi.org/10.1080/17415977.2016.1169279

ORIGINAL ARTICLE

A Three-dimensional Image Reconstruction Algorithm for Electrical Impedance Tomography using Planar Electrode Arrays

Husein Perez[a], Michael Pidcock[a] and Cristiana Sebu[a,b] *

[a] *Department of Mechanical Engineering and Mathematical Sciences, Oxford Brookes University, Wheatley Campus, Oxford OX33 1HX, United Kingdom*
[b] *Department of Mathematics, Faculty of Science, University of Malta, Msida MSD 2080, Malta*

(*March 2016*)

We present a three-dimensional non-iterative reconstruction algorithm developed for conductivity imaging with real data collected on a planar rectangular array of electrodes. Such an electrode configuration as well as the proposed imaging technique are intended to be used for breast cancer detection. The algorithm is based on linearizing the conductivity about a constant value and allows real-time reconstructions. The performance of the algorithm was tested on numerically simulated data and we successfully detected small inclusions with conductivities three or four times the background lying beneath the data collection surface. The results were fairly stable with respect to the noise level in the data and displayed very good spatial resolution in the plane of electrodes.

Keywords: Electrical Impedance Tomography (EIT); planar electrode arrays; breast cancer detection; image reconstruction; inverse problem; ill-posed problem; linearisation

AMS Subject Classifications: 31B10; 45Q05; 47A52; 65F20; 65F22

1. Introduction

Electrical Impedance Tomography (EIT) is a technology used to image the distribution of electrical properties such as conductivity and/or permittivity within an object using measurements of electric currents and voltages on its surface. Since different materials display different electrical properties, EIT can be used as a method of industrial, geophysical and medical imaging (see, for example, [1] and the references therein). The application of EIT considered in this paper is breast cancer imaging.

Breast cancer is routinely investigated by palpation, X-ray mammography or ultrasound imaging with sensitivity rates of up to 90%. The diagnoses, however, yield rather unspecific results. Only one in five biopsies of suspicious lesions leads to a malignant histological diagnosis [2], causing unnecessary distress for the patient and significant delays in establishing a diagnosis. Research is therefore aimed at developing alternative imaging techniques to diagnose malignant breast tumours more accurately and possibly earlier. Since *in vivo* studies have discovered a difference of three times or more in the specific electrical conductivity and permittivity between healthy and cancerous tissue [3–5], imaging the electrical properties of breast tissues could improve the specificity of mammograms. The advantages (portability, low cost, little or zero patient discomfort, no known patient risk and no known side effects) of an impedance imaging

*Corresponding author. Emails: csebu@brookes.ac.uk, cristiana.sebu@um.edu.mt

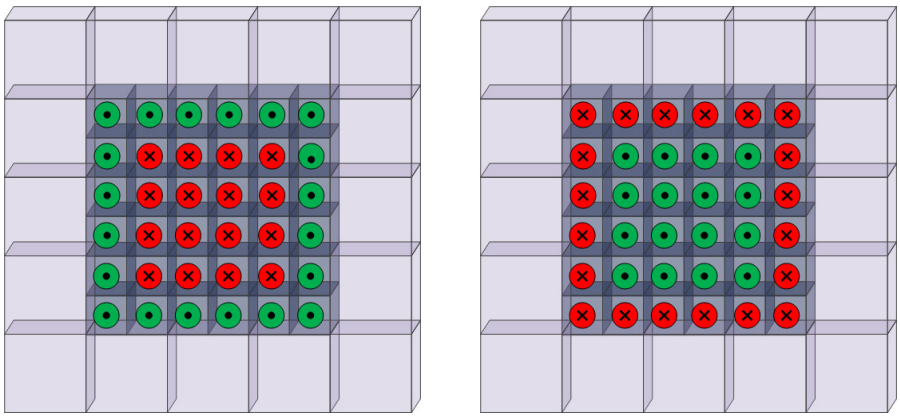

(a) Real experimental setup (b) Thought experimental setup

Figure 1. Layout of the rectangular electrode array of the latest prototype developed at the University of Mainz in collaboration with Oxford Brookes University: ● are the active electrodes used for current injection, and ⊗ are the passive electrodes used for potential measurements.

system over traditional X-ray mammography could make this technology a welcome addition to the tools available in the fight against breast cancer. Although much research has been devoted to both the theoretical and the practical developments of Electrical Impedance Mammography [6–19], to date, the technique has not reached clinical acceptance because of its sensitivity to measurement errors, high computational demands and practical issues: errors in electrode positions or boundary shape, high and uncontrollable contact impedance of the skin (variations of 20% or more).

Several EIT mammographic sensors have been developed recently at the University of Mainz in collaboration with Oxford Brookes University. In contrast to most previous EIT instruments designed for breast cancer detection [9], but similar to devices studied by [6, 7, 16, 18, 20, 21], these mammographic sensors are planar. Detailed descriptions of earlier prototypes can be found in [22, 23]. The latest design consists of a planar sensing head with 36 disk electrodes of equal size arranged in a rectangular array of 20 outer (active) electrodes where the external currents are injected, and 16 inner (passive) electrodes where the induced voltages are measured, see Figure 1(a). To avoid any problems due to the unknown contact impedance, the voltages are not measured at the active electrodes, but at the passive electrodes, very high impedance voltage measurements are taken, and the problem of the unknown contact impedance does not arise. These voltage measurements are relative to the systems ground. Moreover, the device has a fixed geometry and the positions of the electrodes are exactly known.

Almost all previous EIT devices [6, 7, 9, 16, 18, 20, 21] use the same electrodes for current injection and voltage measurement. The excitation current is injected (extracted) at one pair of electrodes at a time and the resulting voltage is measured at all or some of the remaining electrodes. The novelty of our EIT devices, and hence of the image reconstruction methods proposed consists precisely in the distinct use of active and passive electrodes. The active electrodes are used only for current injection while the passive electrodes only for voltage measurements.

In two-dimensions, two different non-iterative algorithms for imaging the conductivity at the surface using the tomographs designed at the University of Mainz were described in [22, 23]. In both cases numerical reconstructions had very good spatial resolution, and the algorithms were robust with respect to errors in the data. A three-dimensional iterative reconstruction method that enforced sparsity and used an adapted complete electrode model was also applied to these devices in [24]. Although it produced good images, this iterative procedure proved to be quite demanding computationally and sensitive to the choice of the regularization parameter.

The purpose of the current paper is to respond to these issues i.e. the two-dimensional nature of the first two algorithms and the numerical sensitivity of the sparsity algorithm, by developing a simple, direct and rapid three dimensional reconstruction algorithm to image the region beneath the rectangular electrode array. The proposed inversion technique is intended to be used in the future for conductivity imaging using real data collected by the specific EIT device described above. The reconstruction method is similar to an approach described in [21] and is based on linearising the conductivity distribution about a constant approximation in order to reduce the computational demands.

The structure of the paper is as follows. In Section 2, we present the mathematical formulation of the inverse problem and of the method proposed to image the conductivity. Section 3 is dedicated to the numerical implementation of the reconstruction algorithm. The performance of the algorithm is illustrated by showing a number of reconstructions from simulated data in Section 4.

2. Mathematical formulation

Since the EIT sensor is much smaller than the human body to which it is applied, and given the rapid decay of the induced potentials as we move away from the top surface (see equation (3)), the mathematical analysis of breast cancer detection can be considered to be the inverse conductivity problem of EIT on an unbounded domain, specifically the lower half space. Let $\Omega = \{(x, y, z) : z < 0\} \in \mathbb{R}^3$ be a conductive object with boundary $\Gamma = \{(x, y, z) : z = 0\}$ and $Q \subset L^\infty(\Omega)$ be a set of uniformly strictly positive parameters. Suppose that $\sigma \in Q$ is an isotropic scalar electrical conductivity distribution and that there are no current sources inside Ω. A set of L electrodes is placed on Γ in a rectangular array. Let $\{e_l\}_{l=1}^{M}$ be the set of passive electrodes (voltage measurement) and $\{e_l\}_{l=M+1}^{L}$ be the active electrodes (current injection). If low-frequency currents are applied to the active electrodes, the electric potential u satisfies the generalized Laplace equation

$$\nabla \cdot (\sigma(x, y, z)\nabla u(x, y, z)) = 0 \quad \text{in} \quad \Omega\,, \tag{1}$$

subject to the boundary condition

$$\sigma(x, y, 0)\frac{\partial u}{\partial z}(x, y, 0) = j(x, y) \quad \text{on} \quad \Gamma, \tag{2}$$

where j is the induced current density distribution.

In this paper we restrict our analysis to currents $j \in \mathcal{L}^2_\diamond(\Gamma)$ with bounded support and to weak solutions $u \in \mathcal{H}$ of equation (1) in the lower half-space Ω for which the following point-wise estimates hold uniformly with respect to the direction of $\mathbf{x} = (x, y, z)$:

$$|u(\mathbf{x})| = \mathcal{O}(1/\|\mathbf{x}\|) \qquad \text{as} \quad \|\mathbf{x}\| \to \infty\,, \tag{3}$$

and

$$\left|\frac{\partial u}{\partial \zeta}(\mathbf{x})\right| = \mathcal{O}(1/(\|\mathbf{x}\|)) \qquad \text{as} \quad \|\mathbf{x}\| \to \infty \quad \text{for} \quad \zeta = x,\, y,\, z\,. \tag{4}$$

Here, $\mathcal{L}^2_\diamond(\Gamma)$ denotes the space of L^2-functions with vanishing integral mean on Γ and $\mathcal{H} = H^{1,\alpha}(\Omega)$ is a completion of suitable C^∞-functions with respect to the norm $\|\cdot\|_{1,\alpha}$ parametrised

by the weight function $\rho_\alpha(x,y,z) = (1+\|\mathbf{x}\|)^\alpha$ with $\alpha > 1$. Further details on the definition of the weighted Sobolev spaces $H^{1,\alpha}(\Omega)$ and on the derivation of these asymptotic estimates can be found in [25].

The weak formulation for the boundary value problem (1)-(2) and its properties are well known. However, we will use the same formulation as in [25], i.e. a function $u \in \mathcal{H}$ is called a weak solution of this Neumann boundary problem if

$$T(\sigma, u, v) = L_j(v), \quad \text{for any} \quad v \in \mathcal{H}\,, \tag{5}$$

where the trilinear form $T : L^\infty(\Omega) \times \mathcal{H} \times \mathcal{H} \to \mathbb{R}$ and the linear form $L_j : \mathcal{H} \to \mathbb{R}$ are defined by

$$T(\sigma, u, v) = \int_\Omega \sigma \nabla u \cdot \nabla v \, dV\,, \tag{6}$$

$$L_j(v) = \int_\Gamma j v \, dS\,. \tag{7}$$

Hence, the solution of the Neumann boundary value problem (1)-(2) is given by $u = T_\sigma^{-1} L_j$, where $T_\sigma^{-1} \in L(\mathcal{H}^*, \mathcal{H})$, the inverse of $T(\sigma,\cdot,\cdot)$, exists and is bounded and continuous [26, 27].

Since in our application the voltages are not measured at the active electrodes, the ave-gap electrode model [12] can be used. We, therefore, assume that the current density is uniformly distributed over each active electrode and that it is zero outside of the support of all active electrodes. Hence, we approximate j in equation (2) by

$$j(x,y) = \begin{cases} I_l/A_l\,, & (x,y) \quad \text{on} \quad e_l\,, \quad l = M+1,\ldots,L \\ 0\,, & \text{otherwise}\,, \end{cases} \tag{8}$$

where I_l is the current sent to the lth active electrode e_l and A_l is the area of e_l.

In our experimental setup, a basis of current patterns $\{\mathbf{I}^1,\ldots,\mathbf{I}^{L-M-1}\}$ is applied to the set of $L-M$ active electrodes $\{e_l\}_{l=M+1}^L$. For each current pattern $\mathbf{I}^k = \left(I_{M+1}^k,\ldots,I_L^k\right)$, $k = 1,\ldots,L-M-1$, the resulting potentials $\mathbf{U}^k = \left(U_1^k,\ldots,U_M^k\right)$ are measured at the set of M passive electrodes $\{e_l\}_{l=1}^M$. The ave-gap model predicts the voltage measured on each electrode as the average of the solution u^k to (1), (2) and (8) with $j = j^k$ over the surface of the electrode:

$$U_l^k = \frac{1}{A_l}\int_{e_l} u^k(x,y,0) dS\,, \quad l = 1,\ldots,M\,. \tag{9}$$

The inverse problem is to estimate the conductivity $\sigma(x,y,z)$ from all $L-M-1$ linearly independent sets of surface measurements.

The reconstruction algorithm presented in this paper is based on the assumption that the spatially varying conductivity is a small perturbation from a constant and known background conductivity σ_0, i.e.

$$\sigma(x,y,z) = \sigma_0 + \delta\sigma(x,y,z)\,, \tag{10}$$

where $\sigma = \sigma_0$ near Γ. Let us also express the corresponding potential u in terms of u_0, the

solution of (1), (2) and (8) for $\sigma = \sigma_0$, as

$$u(x, y, z) = u_0(x, y, z) + \delta u(x, y, z)\,. \tag{11}$$

It is shown in [26, 27] that both the parameter-to-solution map

$$A_\sigma : Q \to \mathcal{H}\,, \quad \sigma \mapsto T_\sigma^{-1} L_j\,. \tag{12}$$

and the complete parameter-to-solution map (i.e. forward operator for a single measurement with current density j)

$$A_j : Q \to \mathcal{L}^{2,\alpha}_\diamond(\Gamma)\,, \quad \sigma \mapsto \gamma \circ T_\sigma^{-1} L_j\,, \tag{13}$$

are analytic on each uniformly strictly positive open set Q. It therefore follows that $\delta u = \mathcal{O}(\delta\sigma)$ in $\overline{\Omega}$. Here, $\gamma : \mathcal{H} \to \mathcal{L}^{2,\alpha}_\diamond(\Gamma)$ is the trace operator and $\mathcal{L}^{2,\alpha}_\diamond$ is the weighted $\mathcal{L}^2_\diamond$-space with respect to ρ_α.

Our method now follows the approach of Calderón [28]. Inserting equations (10) and (11) into (1) and simplifying leads to the following linearised equation

$$\nabla \cdot \sigma_0 \nabla \delta u + \nabla \cdot \delta\sigma \nabla u_0 = \mathcal{O}(\delta\sigma)\ . \tag{14}$$

We choose a test function $v_0 \in \mathcal{H}$ that is the solution of the following boundary value problem:

$$\nabla \cdot (\sigma_0 \nabla v_0(x, y, z)) = 0, \quad \text{in} \quad \Omega, \tag{15}$$

$$\sigma_0 \frac{\partial v_0}{\partial z}(x, y, 0) = \tilde{j}(x, y) = \begin{cases} \tilde{I}_l / A_l\,, & (x, y) \quad \text{on} \quad e_l\,, \quad l = 1, \ldots, M \\ 0\,, & \text{otherwise}\,, \end{cases}, \tag{16}$$

where $\tilde{I}_l$ is a simulated current applied at the lth passive electrode. More explicitly, u_0 is the (weak) potential created in Ω if it consisted of a material of constant conductivity σ_0, while v_0 is the induced (weak) potential when currents are applied to this object of uniform conductivity distribution but reversing the roles of the active and passive electrodes. An illustration of the thought experimental setup corresponding to the homogeneous forward problem (15)-(16) is presented in Figure 1(b). There are $M - 1$ linearly independent simulated current patterns $\{\tilde{\mathbf{I}}^1, \ldots, \tilde{\mathbf{I}}^{M-1}\}$, where $\tilde{\mathbf{I}}^i = \left(I_1^i, \ldots, I_M^i\right)$, that can be applied to the M passive electrodes.

We now multiply the expression in equation (14) by this test function v_0 and integrate over Ω. Applying Gauss's divergence theorem [29] and taking into account the asymptotic behaviour of weak solutions of (1) and (15) given by equations (3)-(4) yields

$$\int_\Gamma \mathbf{n} \cdot v_0 \left(\sigma_0 \nabla \delta u + \delta\sigma \nabla u_0\right)\, dS = \int_\Omega \left(\sigma_0 \nabla v_0 \cdot \nabla \delta u + \delta\sigma \nabla v_0 \cdot \nabla u_0\right)\, dV + \mathcal{O}(\delta\sigma)\,, \tag{17}$$

where $\mathbf{n}$ is the outward normal unit vector.

Furthermore, multiplying equation (15) by $\delta u \in \mathcal{H}$ and repeating the same steps as above, we obtain

$$\int_\Gamma \mathbf{n} \cdot \left(\sigma_0 \delta u_0 \nabla v_0\right)\, dS = \int_\Omega \sigma_0 \nabla \delta u \cdot \nabla v_0\, dV\,. \tag{18}$$

Inserting this result in equation (17) gives

$$\int_\Gamma \mathbf{n}\cdot v_0\,(\sigma_0\nabla\delta u+\delta\sigma\nabla u_0)\;dS=\int_\Gamma \mathbf{n}\cdot(\sigma_0\delta u\nabla v_0)\;dS+\int_\Omega \delta\sigma\nabla v_0\cdot\nabla u_0\,dV+\mathcal{O}(\delta\sigma)\,. \quad (19)$$

Since both u and u_0 satisfy the same Neumann boundary condition (2), it follows that $\mathbf{n}\cdot\,(\sigma_0\nabla\delta u+\delta\sigma\nabla u_0)|_\Gamma+\mathcal{O}(\delta\sigma)=0$ and equation (19) becomes

$$\int_\Gamma \mathbf{n}\cdot(\sigma_0\delta u\nabla v_0)\;dS=-\int_\Omega \delta\sigma\nabla v_0\cdot\nabla u_0\,dV+\mathcal{O}(\delta\sigma)\,. \quad (20)$$

Within this setting, for fixed Neumann data $\mathbf{n}\cdot\,\sigma_0\nabla u_0|_\Gamma=j$, equation (20) expresses in weak form the change in the Neumann-to-Dirichlet map which occurs due to a change in σ_0 for some test function $v_0\in\mathcal{H}$ that is the solution of equation (15) with Neumann trace $\mathbf{n}\cdot\,\sigma_0\nabla v_0|_\Gamma=\tilde{j}\in\mathcal{L}^2_\diamond(\Gamma)$.

Equation (20) is true for any u^k and u_0^k, (weak) solutions of equation (1) for a given current pattern j^k applied to the active electrodes, and for any v_0^i, (weak) solution of equation (15) subject to a current density $\tilde{j}^i$ corresponding to the i-th simulated current pattern $\tilde{\mathbf{I}}^i$ applied at the passive electrodes and given by equation (16). Thus, the linearised problem (20) can be approximated by the following system of equations

$$\begin{aligned}\sum_{l=1}^{M}\int_{e_l}\left(u_0^k-u^k\right)\tilde{j}^i\,dS\;&\approx\;\int_\Omega\delta\sigma\nabla v_0^i\cdot\nabla u_0^k\,dV\,,\\ &\qquad k=1,\ldots,L-M-1\quad\text{and}\quad i=1,\ldots,M-1\,. \quad (21)\end{aligned}$$

Using the ave-gap model for the electrodes, the inverse problem becomes that of finding the perturbation $\delta\sigma$ satisfying the following system of equations

$$\begin{aligned}\sum_{l=1}^{M}\left(U_{0,l}^k-U_l^k\right)\tilde{I}_l^i\;&=\;\int_\Omega\delta\sigma\nabla v_0^i\cdot\nabla u_0^k\,dV\,,\\ &\qquad k=1,\ldots,L-M-1\quad\text{and}\quad i=1,\ldots,M-1\,, \quad (22)\end{aligned}$$

where

$$U_{0,l}^k=\frac{1}{A_l}\int_{e_l}u_0^k(x,y,0)dS\,. \quad (23)$$

The left-hand side of (22) contains only measured and simulated quantities, U_l^k and $U_{0,l}^k$, respectively, and will be denoted by $B(i,k)$, i.e.

$$B(i,k)=\sum_{l=1}^{M}\left(U_{0,l}^k-U_l^k\right)\tilde{I}_l^i\,. \quad (24)$$

A further simplification that can be introduced to aid the image reconstruction process comes from the fact that our objective is to identify a small object(tumour) of uniform conductivity lying within a region (breast tissue) of uniform, but different and known, conductivity. We may

therefore assume that the conductivity is piecewise constant. In this case the half-space can be approximated by voxels, $\{V_n\}_{n=1}^{\infty}$, and thus

$$\delta\sigma(x,y,z) = \sum_{n=1}^{\infty} \delta\sigma_n \chi_n(x,y,z)\,,$$

where χ_n is the characteristic function over the nth voxel, i.e.

$$\chi_n(x,y,z) = \begin{cases} 1\,, & (x,y,z) \in V_n\,, \\ 0\,, & \text{otherwise}\,, \end{cases}$$

However, in practice, we only have a finite number of measurements and, hence, we can reconstruct the conductivities of a finite number N of voxels, where $N \leq (L-M-1)\times(M-1)$. In this case, equation (22) reduces to an over-determined linear system of equations

$$B(i,k) = \sum_{n=1}^{N} A(i,k,n)\delta\sigma_n\,, \quad k = 1,\ldots,L-M-1 \quad \text{and} \quad i = 1,\ldots,M\,, \tag{25}$$

where

$$A(i,k,n) = \int_{V_n} \nabla v_0^i \cdot \nabla u_0^k \, dV\,. \tag{26}$$

Note that the matrix $\mathbf{A}$ is independent of the measured voltage data and it can be computed in advance and stored for use with other reconstructions in the same geometry.

Since, the linearized system of equations (25) inherits ill-posedness from the original nonlinear inverse conductivity problem, the matrix $\mathbf{A}$ is ill-conditioned and regularization is required. The system of equations (25) is therefore solved by means of generalized inverse and truncated singular value decomposition was used as the regularization scheme [31]. In this way very small singular values (i.e. smaller than a certain threshold ϵ) will be neglected and will not enter in the reconstruction.

3. Numerical implementation

3.1. *Electrode and voxel configuration*

As described earlier, our planar array of electrodes is rectangular and consists of $L\,(=36)$ circular electrodes of radius $r_l\,(=3.5\text{mm})$, $l = 1,\ldots,L$, which are equally spaced. The distance between the centres of two adjacent electrodes is $d\,(=12\text{mm})$. There are $M\,(=16)$ passive (inner) electrodes and $L-M\,(=20)$ active (outer) electrodes. The terms outer and inner are relative to the positions of the electrodes in the array. As seen in Figure 1(a), all the electrodes located on the boundary of the rectangular array are active, while the remaining ones are passive. At this point, it is important to note that this electrode configuration not only provides a simpler geometry than the hexagonal pattern of the earlier prototypes in [22, 23], but for some electrical impedance imaging problems in geophysics, archaeology, medical diagnosis and industrial plant control, an appropriate electrode geometry may be that of a rectangular array of electrodes placed on a surface plane. For example, rectangular electrode configurations have been employed before for medical applications such as: breast cancer detection [6, 7, 21, 32],

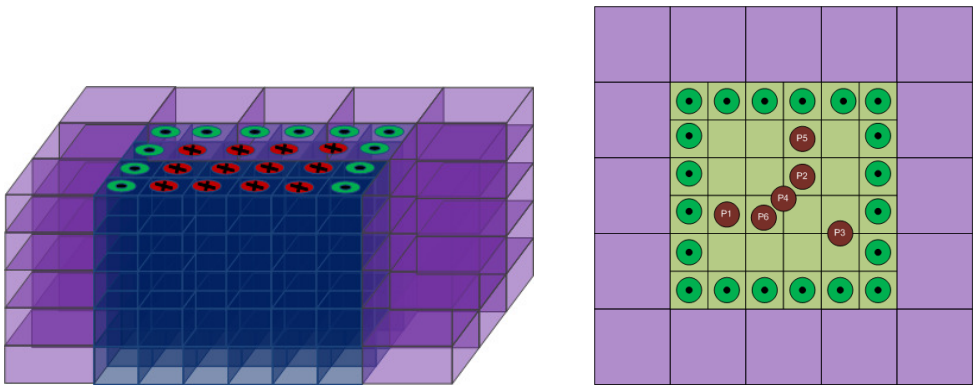

(a) Three-dimensional view (b) Two-dimensional view

Figure 2. Voxel configuration: ⊙ are the active electrodes, ⊗ are the passive electrodes, and $P1 - P5$ denote the positions in the xy-plane where inclusions were placed in our numerical simulations.

respiratory monitoring, functional imaging of the digestive system and peripheral venography [33], or for engineering and environmental studies (e.g. [34] and the references therein).

For the numerical implementation of our algorithm, we use a layered voxel configuration similar to the one introduced in [21] and it is depicted in Figure 2(a). There are 52 inner voxels in each layer:

> 36 small inner voxels aligned immediately under the electrodes of dimensions 12mm $\times$ 12mm $\times$ 2mm, and
>
> 16 outer large voxels arranged around the boundary of the electrode array of dimensions 24mm $\times$ 24mm $\times$ 2mm (i.e. the same height, 2mm, but four times the volume of a small voxel).

Although our interest is to image the conductivity in the region under the electrode array, the voxel configuration has to model, nevertheless, an unbounded domain. The reason for introducing the outer large voxels is to achieve this in a practical manner. As mentioned in Section 2, the total number of voxels should satisfy $N \leq (L - M - 1) \times (M - 1) = 285$. Hence, since there are 52 voxels per layer, we cannot consider more than 5 layers of voxels (i.e. $N = 5 \times 52 = 260 \leq 285$). Note that the number of voxels per layer is determined by the geometry of the electrode array, while the total number of layers is constrained by the number of active and passive electrodes, i.e. the total number (=285) of possible combinations of measured and simulated currents. The height of each voxel layer, however, is not fixed and it can be adjusted to allow conductivity reconstructions up to the required depths. Most of breast tumours are located near the skin surface [35]. The results of a clinical study of single-breast lesions located at least 0.5cm from the skin surface and pectoralis margin and at least 2.0cm from the nipple showed that the mean distance from the skin surface to the lesion was 0.9cm (range, $0.5 - 1.7$cm) [36]. Therefore, in this approach we chose a voxel configuration which allows reconstructions up to a depth of 1cm (=5 layers$\times$2mm).

3.2. *Computation of matrix* **A**

Before we discuss the construction of matrix $\mathbf{A}$ in (26), we need to address the problem of computing the potentials u_0 and v_0 for a homogeneous medium.

Let $P = (x, y, z)$ be an interior point in Ω, $Q_0 = (x', y', 0)$ be a point on the boundary Γ and $Q_l = (x_l, y_l, 0)$ be the centre of lth electrode. For a constant conductivity distribution σ_0, the

solutions of the two theoretical forward problems, defined by (1), (2) and (8) with $j = j^i$ and (15)-(16) with $\tilde{j} = \tilde{j}^k$, are straightforward [29]:

$$\begin{aligned} u_0^k(x,y,z) &= \frac{1}{2\pi\sigma_0}\int_\Gamma \frac{1}{r_{PQ_0}} j^k(x',y')\,dx'\,dy' \\ &= \frac{1}{2\pi\sigma_0}\sum_{l'=M+1}^{L}\frac{I_{l'}^k}{A_{l'}}\int_{e_{l'}}\frac{1}{r_{PQ_0}}\,dx'\,dy'\,, \quad k=1,\ldots,L-M-1\,, \end{aligned} \tag{27}$$

and, respectively,

$$\begin{aligned} v_0^i(x,y,z) &= \frac{1}{2\pi\sigma_0}\int_\Gamma \frac{1}{r_{PQ_0}} \tilde{j}^i(x',y')\,dx'\,dy' \\ &= \frac{1}{2\pi\sigma_0}\sum_{l=1}^{M}\frac{\tilde{I}_l^i}{A_l}\int_{e_l}\frac{1}{r_{PQ_0}}\,dx'\,dy'\,, \quad i=1,\ldots,M-1\,, \end{aligned} \tag{28}$$

where $r_{PQ_0} = |P - Q_0| = \sqrt{(x-x')^2 + (y-y')^2 + z^2}$.

In order to compute the entries of the matrix $\mathbf{A}$, we have to discretize the volume integral in (26). To this end, we follow the same approach as in [21] and we divide each of the voxels into m subvoxels V_n^j ($j = m = 1$ for the inner voxels and $j = 1, ..., m = 4$ for the outer ones). Thus, there will be 100 subvoxels of equal volume per layer. The volume of the jth subvoxel of the nth voxel V_n^j is, therefore, $Vol_n^j = 12 \times 12 \times 2 = 288\text{mm}^3$. Using this dicretization, and the expressions for u_0^k and v_0^i given by equations (27) and (28), we obtain the following expression for the entries of the matrix $\mathbf{A}$ by evaluating the integral (26) at the points P_n^j, the centres of subvoxels V_n^j:

$$\begin{aligned} A(i,k,n) = \quad & \sum_{j=1}^{m}\frac{Vol_n^j}{(2\pi\sigma_0)^2}\sum_{l=1}^{M}\sum_{l'=M+1}^{L}\frac{\tilde{I}_l^i I_{l'}^k}{A_l A_{l'}}\times \\ & \left[\nabla_P\int_{e_l}\frac{1}{r_{PQ_0}}dx'\,dy'\right]_{P=P_n^j}\cdot\left[\nabla_P\int_{e_{l'}}\frac{1}{r_{PQ_0}}dx'\,dy'\right]_{P=P_n^j}. \end{aligned} \tag{29}$$

In order to evaluate these entries, we have to compute

$$\nabla_P\int_{e_l}\frac{1}{r_{PQ_0}}dx'\,dy' = \nabla_P\int_{e_l}\frac{1}{|(P-Q_l)-(Q_0-Q_l)|}dx'\,dy'\,, \quad \text{for} \quad l=1,\ldots,L\,. \tag{30}$$

These quantities were computed analytically by converting the integrals to cylindrical coordinates as follows. Let (r,θ,z) and $(s,\vartheta,0)$ be the cylindrical coordinates of $\tilde{P} = P - Q_l$ and $\tilde{Q}_0 = Q_0 - Q_l$, respectively. Specifically, $\tilde{Q} = (\tilde{x},\tilde{y},0)$, where $\tilde{x} = x' - x_l = s\cos(\vartheta)$ and $\tilde{y} = y' - y_l = s\sin(\vartheta)$. Then, r_{PQ_0} can be expressed in cylindrical coordinates as

$$r_{PQ_0} = |\tilde{P} - \tilde{Q}| = \sqrt{r^2 + s^2 - 2rs\cos(\vartheta - \theta) + z^2}\,. \tag{31}$$

It is clear from symmetry that the following integral is independent of the polar angle θ, i.e.

$$\begin{aligned}\int_{e_l} \frac{1}{r_{PQ_0}} dx'\, dy' &= \int_0^{r_l}\int_0^{2\pi} \frac{1}{\sqrt{r^2+s^2-2rs\cos(\vartheta-\theta)+z^2}} s\, ds\, d\vartheta \\ &= \int_0^{r_l}\int_0^{2\pi} \frac{1}{\sqrt{r^2+s^2-2rs\cos\vartheta+z^2}} s\, ds\, d\vartheta\,. \end{aligned} \tag{32}$$

Hence,

$$\nabla_P \int_{e_l} \frac{1}{r_{PQ_0}} dx'\, dy' = \left(\mathbf{e}_r \frac{\partial}{\partial r} + \mathbf{e}_z \frac{\partial}{\partial z}\right) \int_0^{r_l}\int_0^{2\pi} \frac{1}{r_{PQ_0}} s\, ds\, d\vartheta\,, \tag{33}$$

with

$$\frac{\partial}{\partial r} \int_0^{r_l}\int_0^{2\pi} \frac{1}{r_{PQ_0}} s\, ds\, d\vartheta = 2\sqrt{\frac{r_l}{r\kappa}} \left[2E(\kappa) - (2-\kappa)K(\kappa)\right]\,, \tag{34}$$

and

$$\begin{aligned}\frac{\partial}{\partial z} \int_0^{r_l}\int_0^{2\pi} \frac{1}{r_{PQ_0}} s\, ds\, d\vartheta &= \frac{1}{2}\sqrt{\frac{\kappa}{r r_l}} \left[4zK(\kappa) - 2i \times \left((r-r_l-iz)\Pi\left(\frac{2r_l}{r+r_l-iz}\middle|\kappa\right)\right.\right. \\ &+ \left.\left.(-r+r_l-iz)\Pi\left(\frac{2r_l}{r+r_l+iz}\middle|\kappa\right)\right)\right]\,, \end{aligned} \tag{35}$$

where $\kappa = \frac{4rr_l}{(r+r_l)^2+z^2}$, and $K(\kappa)$, $E(\kappa)$ and $\Pi(n|\kappa)$ are the complete elliptic integrals of first, second and third kind, respectively. Further details about these special functions can be found in [38]. Both the r-component and the z-component of the gradient given by equations (34) and (35), respectively, are real valued functions. However, due to numerical inaccuracies in the computer algorithms used to evaluate these functions, there are always some residual imaginary parts in the order of the machine precision. To overcome this issue, only their real parts are considered in further computations.

Note that although in our implementation we preferred to use the above closed form expressions, all these integrals could also be evaluated to great accuracy by using a numerical quadrature method such as boundary elements (see, for example, [37]). This would be more consistent with the numerical experiments where the forward model is a bounded domain but at the cost of increased computation time.

3.3. *Construction of matrix* $\mathbf{B}$

For the construction of matrix $\mathbf{B}$ given by equation (24), we need the measured and simulated voltages, U_l^k and $U_{0,l}^k$, respectively.

In practice, the voltages U_l^k are known experimental data. However, as no real data is yet available, in this paper we simulate the measured voltages numerically as explained in Section 4.

In order to find the values of the simulated voltages $U_{0,l}^k$ given by equation (23), we need to compute first $u_0^k(x,y) = u_0^k(x,y,z=0)$ by evaluating the expression in equation (27) at $z=0$. To this end, we use the same change of variables as in subsection 3.2 and equation (32). Note that due to the symmetry considerations of the integral (32), the solution u_0^k is also independent

of the polar angle θ. Hence, $u_0^k(r,\theta,z=0)=u_0^k(r)$, and we obtain

$$u_0^k(r)=\frac{1}{2\pi\sigma_0}\sum_{l'=M+1}^{L}\frac{I_{l'}^k}{A_{l'}}\int_0^{r_{l'}}\int_0^{2\pi}\frac{1}{\sqrt{r^2+s^2-2rs\cos\vartheta}}s\,ds\,d\vartheta\,,\quad k=1,\ldots,L-M-1\,. \tag{36}$$

The integral in equation (36) can be computed analytically, i.e.

$$\int_0^{r_{l'}}\int_0^{2\pi}\frac{1}{\sqrt{r^2+s^2-2rs\cos\vartheta}}s\,ds\,d\vartheta= 2\,(r+r_{l'})\,E\left(\frac{4\,r\,r_{l'}}{(r+r_{l'})^2}\right)-2\,(r-r_{l'})\,K\left(\frac{4\,r\,r_{l'}}{(r+r_{l'})^2}\right)\,. \tag{37}$$

Once the currents applied at the active electrodes $I_{l'}^k$ are known from measurements, u_0^k can be estimated in a straightforward way using equations (36)-(37) at different points on the surfaces of passive electrodes e_l, $l=1,\cdots,M$, and then obtain $U_{0,l}^k$ by evaluating numerically the integral in equation (23).

The simulated currents $\tilde{\mathbf{I}}^i=\left(\tilde{I}_1^i,\ldots,\tilde{I}_{16}^i\right)$, $i=1,\ldots,M-1=15$, are assumed to be standard linearly independent trigonometric current patterns, i.e.

$$\tilde{I}_l^i=\begin{cases}\cos\left(i(l-1)\frac{2\pi}{M}\right)\,, & i=1,\ldots,\lfloor\frac{M}{2}\rfloor\,,\\ \sin\left(\left(i-\lfloor\frac{M}{2}\rfloor\right)(l-1)\frac{2\pi}{M}\right)\,, & i=\lfloor\frac{M}{2}\rfloor,\ldots,M-1\,,\end{cases} \tag{38}$$

and $l=1,\ldots,M$.

4. Numerical examples

In this section, we present some reconstructions obtained by applying the above reconstruction algorithm to simulated data. The setup of our numerical tests mimicked closely the laboratory experiments presented in [23, 24]. We considered a rectangular tank of length $L\,(=15\text{cm})$, width $W\,(=15\text{cm})$ and height $H\,(=7.5\text{cm})$ which contained an isotropic medium of conductivity approximately equal to that of healthy breast tissue, $\sigma_0=200\text{mS/m}$. The rectangular array of electrodes was placed at the centre of the top of the tank (i.e. $z=0\text{cm}$). The dimensions of the tank were much larger than those of the electrode array (0.72cm$\times$0.72cm) and of the voxel configuration (12cm$\times$12cm$\times$1cm) used for conductivity reconstructions, thus approximating an infinite half space.

Cylindrical inclusions of radii $R_{15}=1.5\text{mm}$, $R_{25}=2.5\text{mm}$ and/or $R_{35}=3.5\text{mm}$, heights $h=5\text{mm}$ and conductivities $\sigma=800\text{mS/m}$ or 600mS/m were then placed on below positions $P1-P5$ in the xy-plane (see Figure 2(b)) and at different depths z. Note that the largest cylindrical object R_{35} has the same radius as the electrodes, while the other two, R_{25} and R_{15}, have much smaller radii. $P1$, $P2$ and $P5$ in Figure 2(b) are positions directly below a passive electrode, while $P4$ and $P5$ are positions between the passive electrodes.

To simulate the measured values of the potential on the boundary we first had to solve the direct problem (1)-(8). In order to avoid inverse crimes and to test the robustness of our inversion techniques we used EIDORS [39] as a forward solver. EIDORS is a finite element software package which has no connection with the reconstruction method under consideration. Current patterns similar to those defined in equation (38) were applied at the active electrodes, $\mathbf{I}^k=\left(I_{21}^k,\ldots,I_{36}^k\right)$, $k=1,\ldots,L-M-1=19$. The direct problem was solved for each of the

nineteen different current patterns and we obtain the values of the corresponding voltages at the passive electrodes $\mathbf{U}^k = \left(U_1^k, \ldots, U_{20}^k\right)$, $k = 1, \ldots, 19$, by interpolating the numerical solution at points on the surface of the electrodes and evaluating numerically the integral in equation (9). This was the data used by our reconstruction algorithm. The conductivities of all $N = 260$ voxels were obtained by inverting the over-determined linear system of equations (25). In the numerical examples considered, singular values smaller than $\epsilon = 10^{-5}$ were cut off (i.e. 35 singular values were used in the reconstructions).

In EIT a noise level of 1% is reasonable in many circumstances, but in some medical applications greater accuracy can be achieved [40]. However, since our reconstruction method is quite stable with respect to the noise level in the data, in all the numerical examples discussed below, we present reconstruction results for data with 2% additive Gaussian random errors. Note that in all figures presented below the colour ranges are the same for each subplot. Moreover, the homogeneity properties of the proposed algorithm are good as, although not displayed here, we were able to reconstruct an uniform distribution of conductivity of 200mS/m using simulated data for the tank with no inclusions.

In Figures 3, 4 and 5, we present the conductivity reconstructions for the medium size cylindrical object of radius R_{25} and conductivity 800mS/m (i.e. four times higher than the background conductivity) placed below position $P1$ (i.e. below an electrode and next to an active electrode) and at depths $z = -2$, -3 and -6mm, respectively, from the array of electrodes. The position of the inclusion in the xy-plane was successfully recovered in all three cases but the reconstructed conductivity values were smaller than the actual conductivity values. This difficulty in recovering the amplitude of high contrast conductivities is a common feature of EIT linearisation methods, see for example [21, 22, 41]. We also found that estimating the depth of the inhomogeneity was more ill-posed than reconstructing its position in the xy-plane. For an inclusion placed at this position, the values of the reconstructed conductivities at position $P1$ were larger in the upper voxel layers with a maximum value attained in the second layer irrespective of the depths of the inclusions. However, the deeper the object, the smaller the values of the reconstructed conductivity. This suggests that some information about the depth location of the inclusions is present in the data, but as seen from Figures 3(f) and 4(f) there is limited information about objects' heights as it seems as if the inclusion extends over all five voxel layers. This conclusion is in agreement with our findings in [24].

To test the spatial resolution of our algorithm, we placed cylindrical inclusions of conductivity 800mS/m and of different radii R_{35}, R_{25} and R_{15} at position $P2$ (i.e. below an electrode, but further away from the active electrodes) and depth $z = -3$mm. The numerical results can be found in Figures 6, 7 and 8, respectively. Similar to the previous numerical experiments, the position of the inclusion in the plane of electrodes was well characterized. The values of the reconstructed conductivities at position $P2$ were also smaller than the true ones, but overall larger in the upper voxel layers with a maximum value attained in the first layer in this case. Moreover, as expected, the smaller the size of the inhomogeneity, the smaller were the values of the reconstructed conductivity. Note that, by using the electrode array and the experimental setup under consideration as well as the proposed three-dimensional reconstruction algorithm, we managed to detect inhomogeneities which are much smaller in size (i.e. a cylinder of radius R_{15} and height 5mm whose conductivity is only four times higher than the background) and up to larger depths than in [21, 23, 24].

When a cylindrical inhomogeneity of radius R_{25} and of conductivity 800mS/m was placed on a position between two electrodes, $P3$, or in the middle of four neighbouring electrodes, $P4$, then the conductivity of all two or four adjacent voxels was much larger than that of the background, see Figures 9 and 10.

Next we demonstrate that the detection of a small conductive inhomogeneity is not affected by the presence of a more resistive tissue layer (i.e. the skin) at the surface. To this end, we

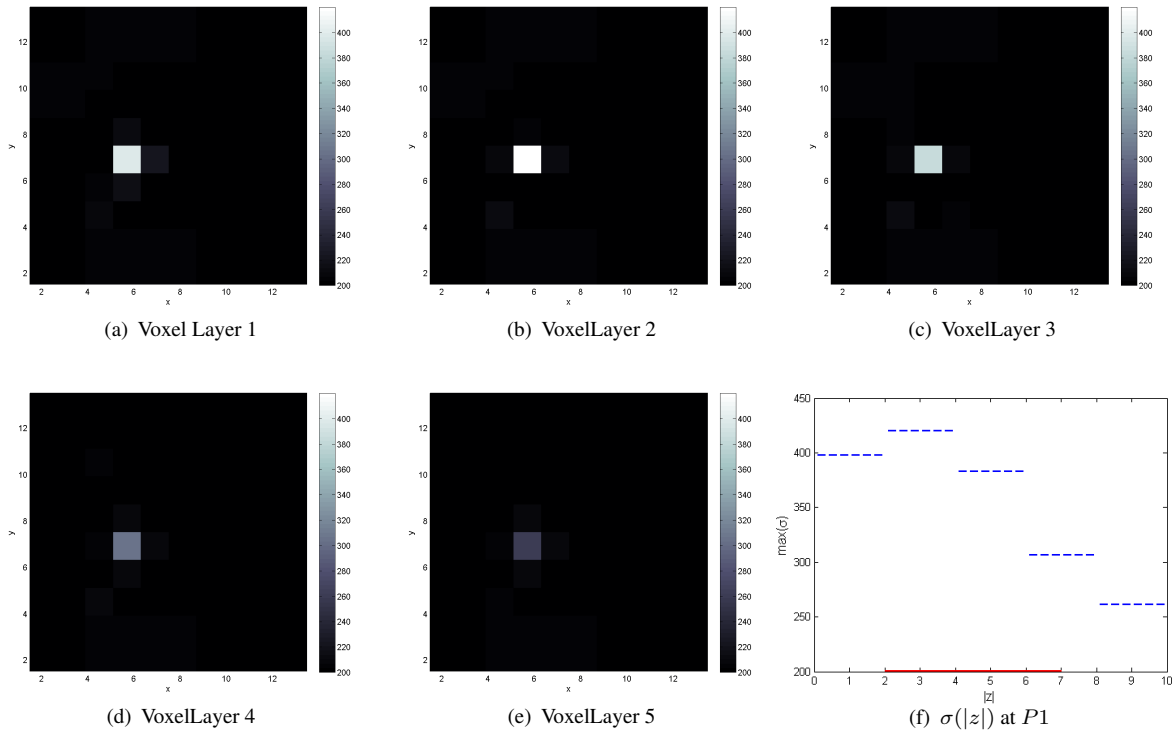

(a) Voxel Layer 1 (b) VoxelLayer 2 (c) VoxelLayer 3

(d) VoxelLayer 4 (e) VoxelLayer 5 (f) $\sigma(|z|)$ at $P1$

Figure 3. Conductivity reconstructions for a cylindrical object of radius R_{25} of conductivity 800mS/m placed at position $P1$ and $z = -2$mm. The thick continuous line in (e) marks the position and the height of the inclusion along the z-axis.

included a 2mm thick resistive layer of conductivity 50mS/m layer directly under the surface. A cylindrical object of radius R_{35} was positioned at $P1$ and $z = -4$mm. As seen from the numerical reconstructions presented in Figure 11, the presence of the object is visible and its position in the xy-plane is well characterized.

The final simulations included in the paper consist of reconstructions of two conductive objects of radii R_{25} and R_{15} placed at positions $P5$ and $P6$, respectively, and at the same depth ($z = -3$mm). Firstly, in Figure 12 we present the results obtained when the two inclusions have the same conductivity (800mS/m). In this case, the presence of the smaller cylindrical object (R_{15}) is slightly shielded by the larger object (R_{25}). Then, in Figure 13 we show the reconstructions of objects of different conductivities (600mS/m and 800mS/m, respectively) when the presence of the smaller object is more pronounced.

5. Conclusion

In this article we have presented a three-dimensional non-iterative reconstruction method developed for conductivity imaging in breast cancer detection using real data from a planar EIT device developed at the University of Mainz in collaboration with Oxford Brookes University. The head of the sensor contains both active electrodes, where standard trigonometric current patterns are applied, and passive electrodes, where the induced voltages are measured, arranged in a rectangular array. A finite region beneath the surface was discretised into voxels of different sizes depending on their position relative to the electrode array and their conductivities were determined from the data measured on the electrode array. The reconstruction algorithm is based

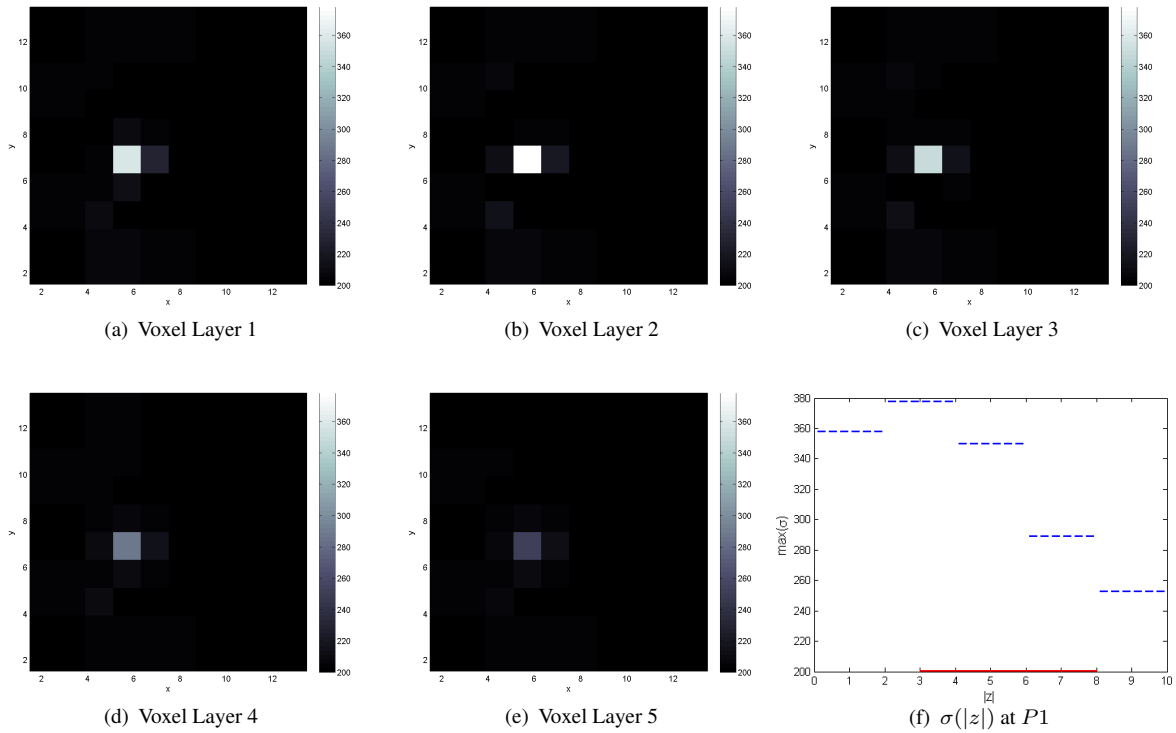

(a) Voxel Layer 1 (b) Voxel Layer 2 (c) Voxel Layer 3

(d) Voxel Layer 4 (e) Voxel Layer 5 (f) $\sigma(|z|)$ at $P1$

Figure 4. Conductivity reconstructions for a cylindrical object of radius R_{25} of conductivity 800mS/m placed at position $P1$ and $z = -3$mm. The thick continuous line in (e) marks the position and the height of the inclusion along the z-axis.

on linearizing the conductivity about a constant value. It is simple, direct and fast, and it allows reconstructions in real-time.

The performance of the algorithm was tested on numerically simulated data. Small inclusions of various conductivities placed at several depths were detected and their positions in the plane of the electrode array were successfully recovered. Although the depth resolution is rather poor, the reconstructions have good spatial resolution in the xy-plane and are quite stable with respect to the noise level in the data. The most relevant feature is the fact that it can detect smaller objects up to larger depths than the other two-dimensional non-iterative approaches developed for similar planar EIT devices in [23, 24]. In future, we plan to obtain reconstructions from real data and try to improve the depth resolution of the algorithm by possibly imposing *a priori* and/or *a posteriori* sparsity constraints on the reconstructed conductivity values in each voxel.

Acknowledgement

The authors would like to express their gratitude to Professor Khaled Hayatleh for a number of useful conversations concerning this work.

References

[1] Borcea L. Electrical Impedance Tomography. Inverse Probl. 2002;18:R99-R136.

[2] Lee CH, Dershaw DD, Kopans D, Evans P, Monsees B, Monticciolo D, Brenner RJ, Bassett L, Berg W, Feig S, Hendrick E, Mendelson E, D'Orsi C, Sickles E, Warren Burhenne L. Breast Cancer

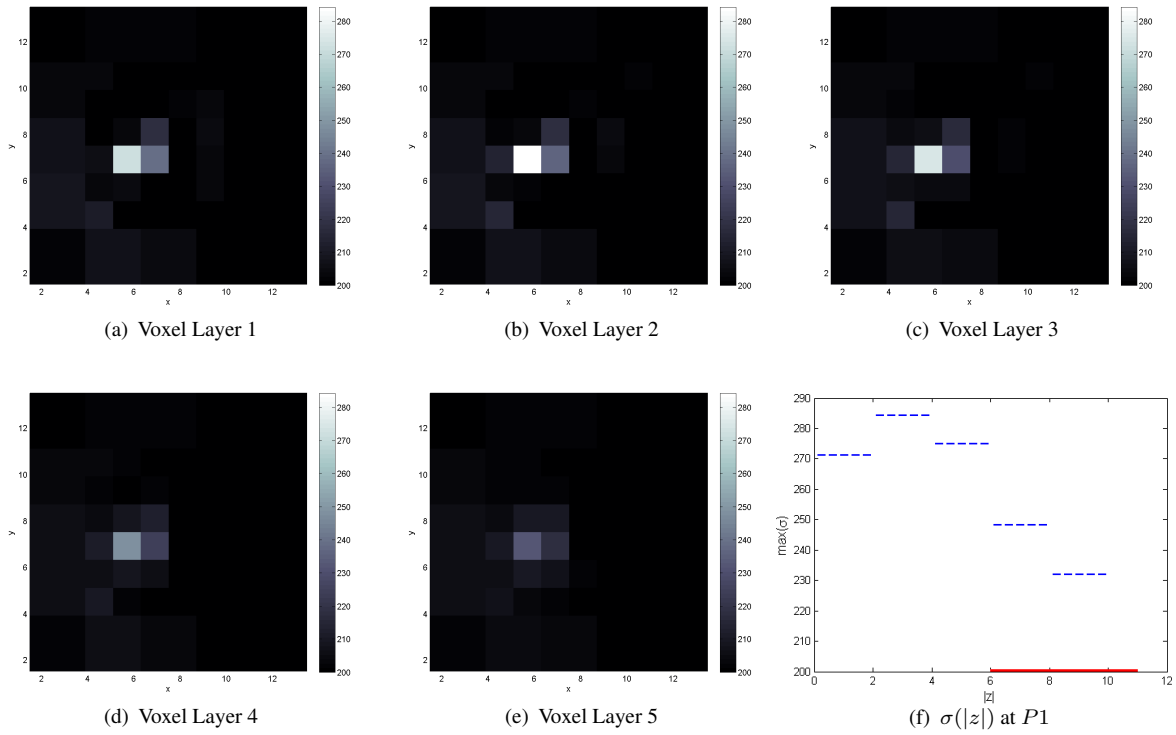

(a) Voxel Layer 1 (b) Voxel Layer 2 (c) Voxel Layer 3

(d) Voxel Layer 4 (e) Voxel Layer 5 (f) $\sigma(|z|)$ at $P1$

Figure 5. Conductivity reconstructions for a cylindrical object of radius R_{25} of conductivity 800mS/m placed at position $P1$ and $z = -6$mm. The thick continuous line in (e) marks the position and the height of the inclusion along the z-axis.

Screening With Imaging: Recommendations From the Society of Breast Imaging and the ACR on the Use of Mammography, Breast MRI, Breast Ultrasound, and Other Technologies for the Detection of Clinically Occult Breast Cancer. J Am Coll Radiol. 2010;7:18-27.

[3] Rigaud B, Morucci JP, Chauveau N. Bioelectrical impedance techniques in medicine. Part I: Bioimpedance measurement. Second section: impedance spectrometry. Crit Rev Biomed Eng. 1996;24:257-351.

[4] Jossinet J. Variability of impeditivity in normal and pathological breast tissue. Med Biol Eng Comput. 1996;34:346-350.

[5] Jossinet J. The impeditivity of freshly excised human breast tissue. Physiol Meas. 1998;19:61-75.

[6] Cherepenin V, Karpov A, Korjenevsky A, Kornienko V, Mazaletskaya A, Mazourov D, Meister D. A 3D electrical impedance tomography (EIT) system for breast cancer detection. Physiol Meas. 2001;22:9-18.

[7] Cherepenin VA, Karpov AY, Korjenevsky AV, Kornienko VN, Kultiasov YS, Ochapkin MB, Tochanova OV, Meister JD, Three-dimensional EIT imaging of breast tissues: system design and clinical testing. IEEE Trans Med Imaging. 2002;21:662-667.

[8] Kerner TE, Paulsen KD, Hartov A, Soho SK, and Poplack SP. Electrical impedance spectroscopy of the breast: clinical imaging results in 26 subjects. IEEE Trans Med Imaging. 2002;21:638-645.

[9] Zou Y, Guo Z. A review of electrical impedance techniques for breast cancer detection. Med End Phys. 2003;25:79-90.

[10] Kim BS, Isaacson D, Xia H, Kao T, Newell J, Saulnier G. A method for analyzing electrical impedance spectroscopy data from breast cancer patients. Physiol Meas. 2007;28:S237-S246.

[11] Poplack SP, Tosteson TD, Wells WA, Pogue BW, Meaney PM, Hartov A, Kogel CA, Soho SK, Gibson JJ, Paulsen KD. Electromagnetic breast imaging: results of a pilot study in women with abnormal mammograms. Radiology. 2007;243:350-359.

[12] Choi MH, Kao T-J, Isaacson D, Saulnier GJ, Newell JC. A reconstruction algorithm for breast cancer

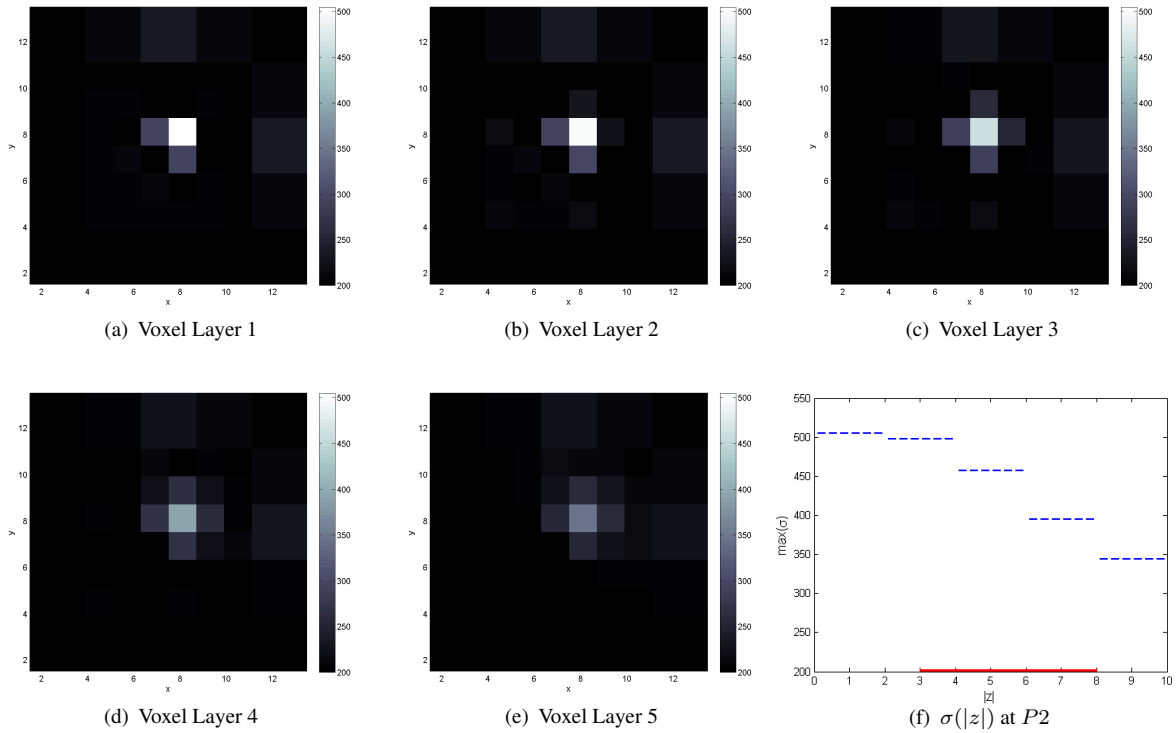

(a) Voxel Layer 1 (b) Voxel Layer 2 (c) Voxel Layer 3

(d) Voxel Layer 4 (e) Voxel Layer 5 (f) $\sigma(|z|)$ at $P2$

Figure 6. Conductivity reconstructions for a cylindrical object of radius R_{35} of conductivity 800mS/m placed at position $P2$ and $z = -3$mm. The thick continuous line in (e) marks the position and the height of the inclusion along the z-axis.

imaging with electrical impedance tomography in mammography geometry. IEEE Trans. Biomed. Eng. 2007;54:700-710.

[13] Trokhanova OV, Okhapkin MB, Korjenevsky AV. Dual-frequency electrical impedance mammography for the diagnosis of non-malignant breast disease. Physiol Meas. 2008;29:S331-S344.

[14] Murphy EK, Isaacson D, Saulnier GJ, Newell JC. Analysis of forward solvers for electrical impedance tomography in a mammography geometry. J Phys Conf Ser. 2010;224:012033.

[15] Ardrey DB, Murphy EK, Isaacson D, Saulnier GJ, Newell JC. Electrical impedance tomography using the finite element method in the mammography geometry. Proc. IEEE 37th Annu. Northeast Bioengineering Conf. 2011;1-2.

[16] Sze G. Detection of Breast Cancer with Electrical Impedance Mammography [PhD Thesis]. Sussex (UK): University of Sussex; 2012.

[17] Pak DD, Rozhkova NI, Kireeva MN, Ermoshchenkova MV, Nazarov AA, Fomin DK, Rubtsova NA. Diagnosis of breast cancer using electrical impedance tomography. Biomed Eng. 2012;46:154-157.

[18] Bilal R. Investigation of undesired errors relating to the planar array system of electrical impedance mammography for breast cancer detection [PhD Thesis]. Sussex (UK): University of Sussex; 2012.

[19] Al Amin A, Parvin S, Kadir MA, Tahmid T, Kaisar Alam S, Siddique-e Rabbani K. Classification of breast tumour using electrical impedance and machine learning techniques. Physiol Meas. 2014;35:965-974.

[20] Azzouz M, Hanke M, Oesterlein C, Schilcher K. The factorization method for electrical impedance tomography data from a new planar device. Int J Biomed Imaging 2007. 2007;7 pages, Article ID 83016.

[21] Mueller JL, Isaacson D, Newell JC. A Reconstruction Algorithm for Electrical Impedance Tomography Data Collected on Rectangular Electrode Arrays. IEEE Trans Biomed Eng. 1999;46:1379-1386.

[22] Hähnlein C, Schilcher K, Sebu C, Spiesberger H. Conductivity imaging with interior potential measurements. Inverse Probl Sc Eng. 2011;19:729-750.

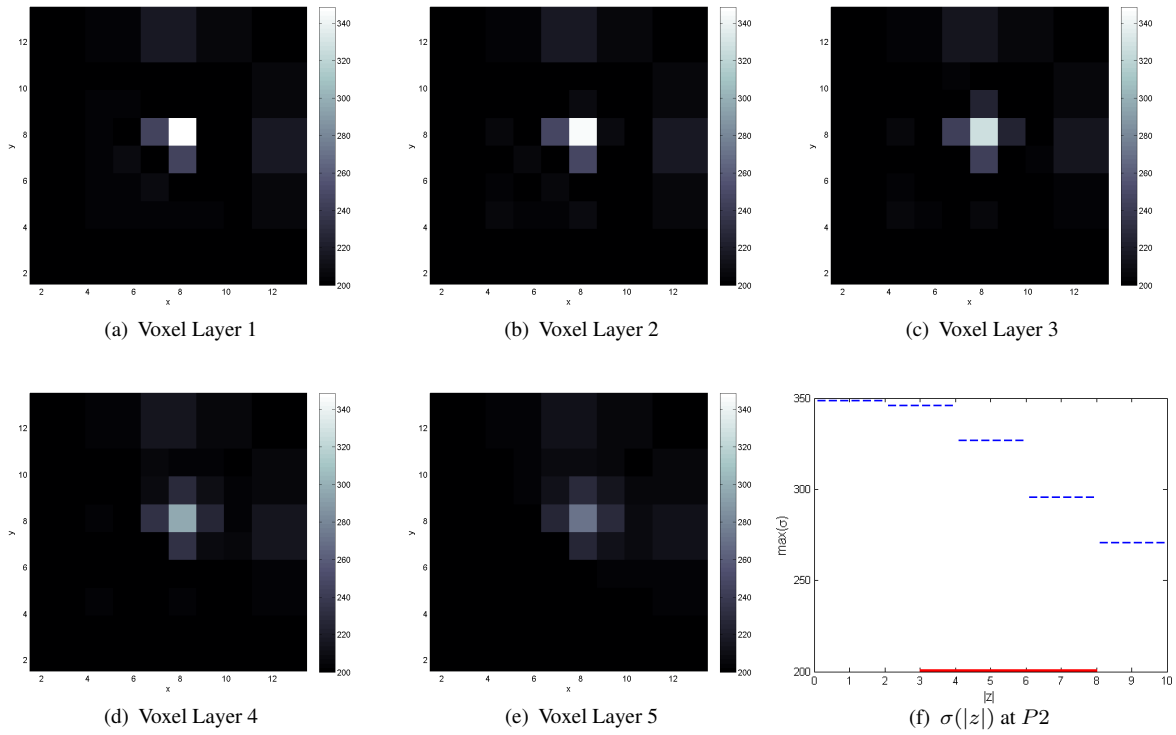

(a) Voxel Layer 1 (b) Voxel Layer 2 (c) Voxel Layer 3

(d) Voxel Layer 4 (e) Voxel Layer 5 (f) $\sigma(|z|)$ at $P2$

Figure 7. Conductivity reconstructions for a cylindrical object of radius R_{25} of conductivity 800mS/m placed at position $P2$ and $z = -3$mm. The thick continuous line in (e) marks the position and the height of the inclusion along the z-axis.

[23] Georgi K-H, Hähnlein C, Schilcher K, Sebu C, Spiesberger H. Conductivity Reconstructions using Real Data from a New Planar Electrical Impedance Device. Inverse Probl Sc Eng. 2013;21:801-822.

[24] Gehre M, Kluth T, Sebu C, Maass P. Sparse 3D reconstructions in Electrical Impedance Tomography using real data. Inverse Probl Sc Eng. 2014;22:31-44.

[25] Lukaschewitsch M, Maass P, Pidcock MK, Sebu C. The asymptotic behaviour of weak solutions to the forward problem of Electrical Impedance Tomography on unbounded three dimensional domains. Math Meth Appl Sc. 2009;32:206-222.

[26] Lukaschewitch M. Inversion of geoelectric boundary data, a non-linear ill-posed problem [PhD Thesis]. Potsdam (Germany): University of Potsdam; 1999.

[27] Lukaschewitch M, Maass P, Pidcock M. Tikhonov regularization for electrica impedance tomography on unbounded domains. Inverse Probl. 2003;19:585-610.

[28] Calderón AP. On an inverse boundary value problem. Sem. Numerical Analysis and its Applications to Continuum Physics. Rio de Janeiro: Sociedade Brasileira de Matematica. 1980; 67-73.

[29] Kervokian J. Partial differential equations: analytical solutions techniques. 2nd ed. New York (US): Springer-Verlag New York; 2000.

[30] Isakov V. Inverse problems for partial differential equations. 2nd ed. New York (US), Springer Science+Business Media, Inc.; 2006.

[31] Hansen PC. Regularization tools: A Matlab package for analysis and solution of discrete ill-posed problems. Numer. Algorithms. 1994;6:1-35.

[32] Assenheimer M, Laver-Moskovitz O, Malonek D, Manor D, Nahaliel U, Nitzan R, Saad A. The T-SCAN^{TM} technology: electrical impedance as a diagnostic tool for breast cancer detection. Physiol Meas. 2001;22:1-8.

[33] Kotre CJ. Subsurface electrical impedance imaging: measurement strategy, image reconstruction and in vivo results. Physiol. Meas. 1996;17:A197-204.

[34] Kemna A, Binley A, Slater L. Crosshole IP imaging for engineering and environmental applications.

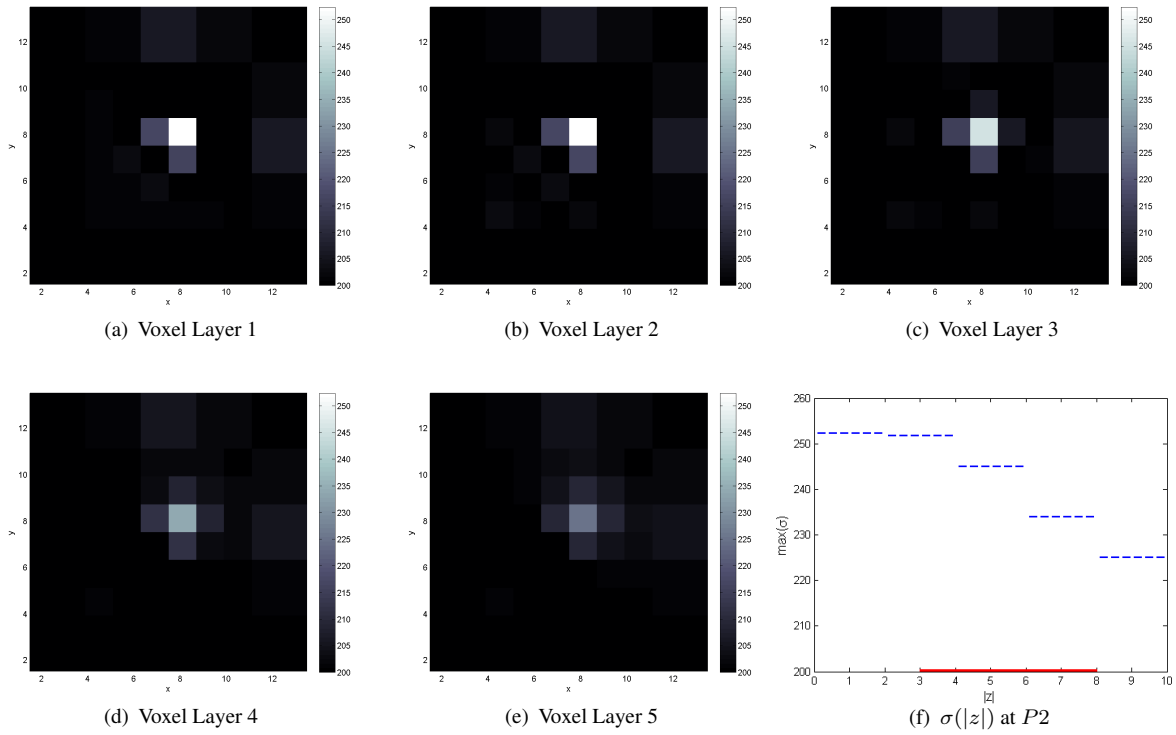

(a) Voxel Layer 1 (b) Voxel Layer 2 (c) Voxel Layer 3

(d) Voxel Layer 4 (e) Voxel Layer 5 (f) $\sigma(|z|)$ at $P2$

Figure 8. Conductivity reconstructions for a cylindrical object of radius R_{15} of conductivity 800mS/m placed at position $P2$ and $z = -3$mm. The thick continuous line in (e) marks the position and the height of the inclusion along the z-axis.

Geophysics. 2004;69:97-107.

[35] Tutt B. New Partial-Breast Radiation Therapy Regimen Uses Protons. Oncolog. 2013;58:4-5.

[36] March D, Coughlin B, Barham R, Goulart R, Klein S, Bur M. Breast masses: removal of all US evidence during biopsy by using a handheld vacuum-assisted device-initial experience. Radiology. 2003;227:549-555.

[37] Brebbia CA, Telles JCF, Wrobel LS. Boundary Element Techniques. Berlin, Germany: Springer-Verlag; 1984.

[38] Gradshteyn IS, Ryzhik M. Table of integrals, series and products. 4th ed. New York (US): Academic Press Inc; 1965.

[39] EIDORS: Electrical Impedance Tomography and Diffuse Optical Tomography Reconstruction Software [computer software]. Available from: http://eidors3d.sourceforge.net/.

[40] Terzopoulos N, Hayatleh K, Hart B, Lidgey FJ, McLeod C. A novel bipolar-drive circuit for medical applications. Physiol Meas 2005;26:N21-N27.

[41] Knudsen K, Lassas M, Mueller J, Siltanen S. Reconstructions of Piecewise Constant Conductivities by the D-bar Method for Electrical Impedance Tomography. J Phys: Conf Ser. 2008;124:012029.

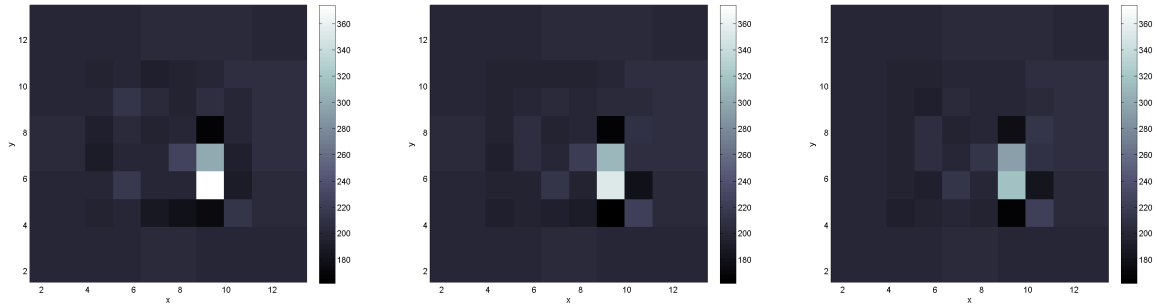

(a) Voxel Layer 1 (b) Voxel Layer 2 (c) Voxel Layer 3

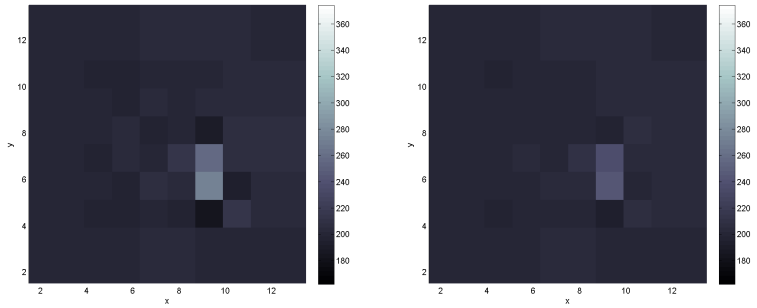

(d) Voxel Layer 4 (e) Voxel Layer 5

Figure 9. Conductivity reconstructions for a cylindrical object of radius R_{25} of conductivity 800mS/m placed at position $P3$ and $z = -3$mm.

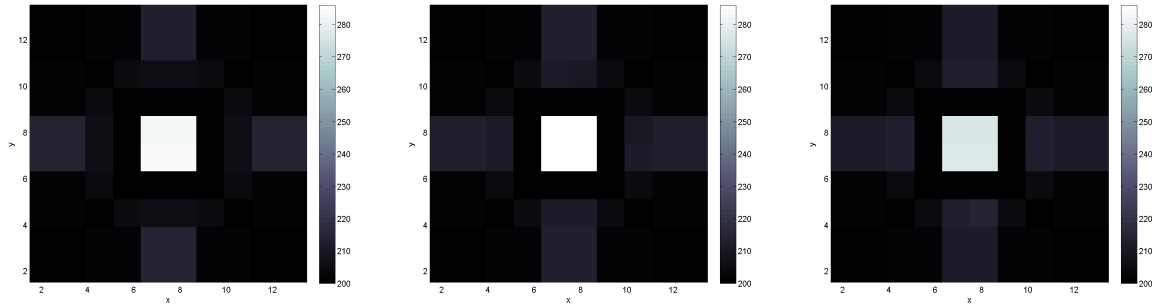

(a) Voxel Layer 1 (b) Voxel Layer 2 (c) Voxel Layer 3

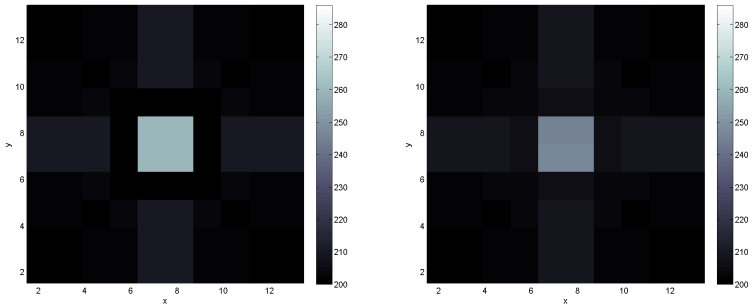

(d) Voxel Layer 4 (e) Voxel Layer 5

Figure 10. Conductivity reconstructions for a cylindrical object of radius R_{25} of conductivity 800mS/m placed at position $P4$ and $z = -3$mm.

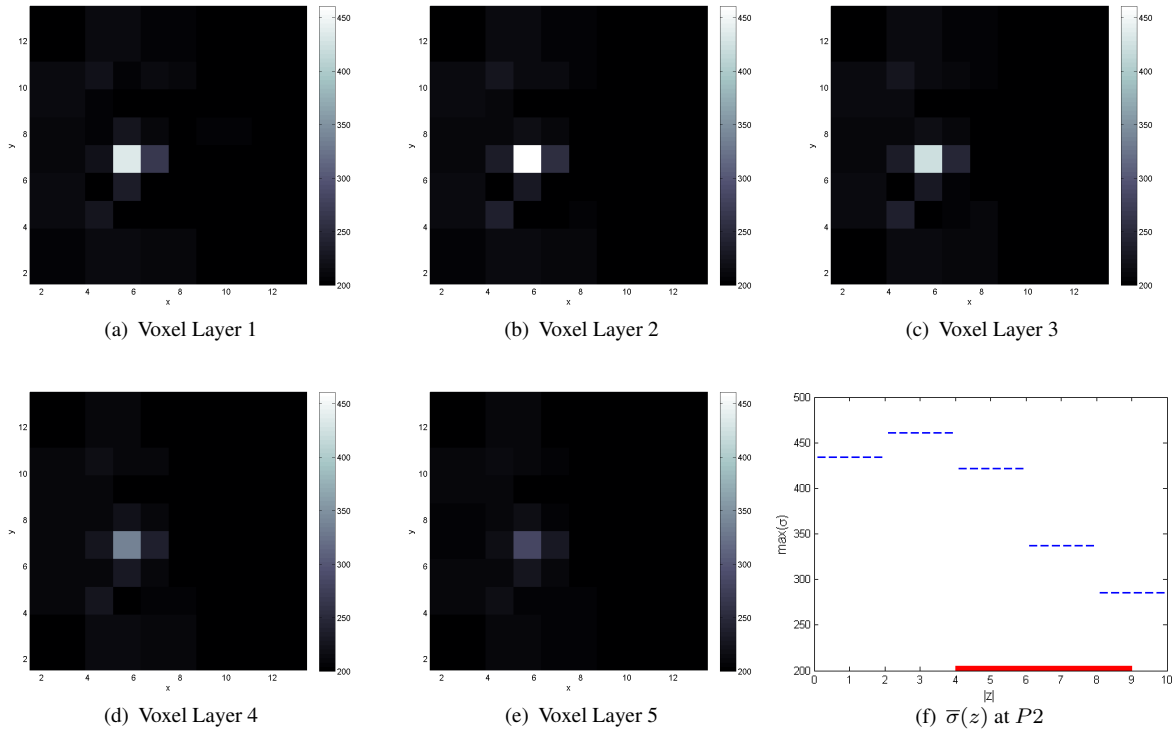

(a) Voxel Layer 1 (b) Voxel Layer 2 (c) Voxel Layer 3

(d) Voxel Layer 4 (e) Voxel Layer 5 (f) $\overline{\sigma}(z)$ at $P2$

Figure 11. Conductivity reconstructions for a cylindrical object of radius R_{35} of conductivity 800mS/m placed at position $P1$ and $z = -4$mm in the presence of a resistive medium (50mS/m) in Voxel Layer 1. The thick continuous line in (e) marks the position and the height of the inclusion along the z-axis.

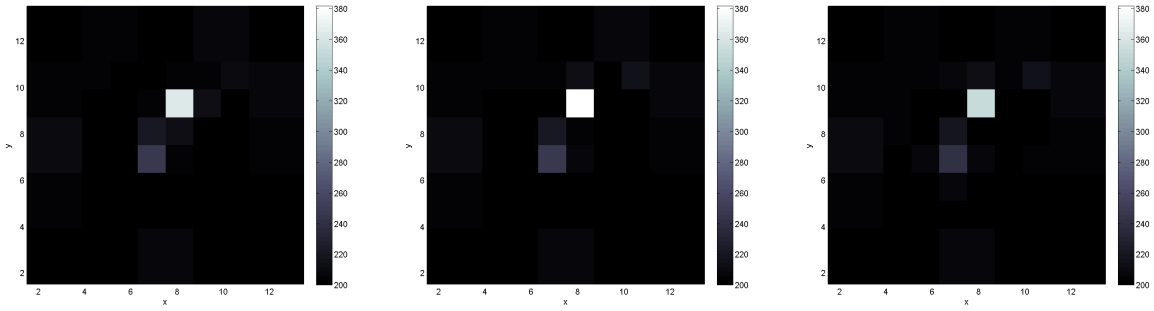

(a) Voxel Layer 1 (b) Voxel Layer 2 (c) Voxel Layer 3

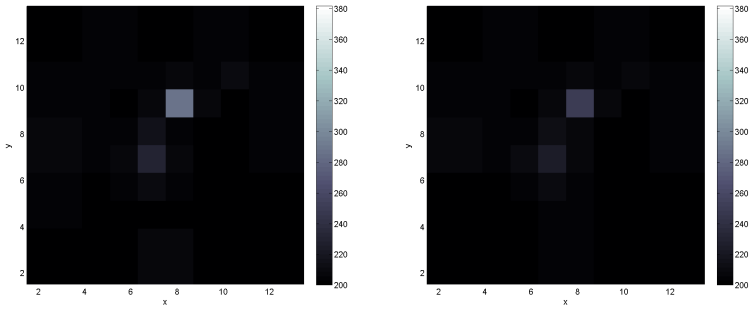

(d) Voxel Layer 4 (e) Voxel Layer 5

Figure 12. Conductivity reconstructions for two cylindrical objects of radii R_{25} and R_{15} of conductivities 800mS/m placed at positions $P5$ and $P6$, respectively, and $z = -3$mm.

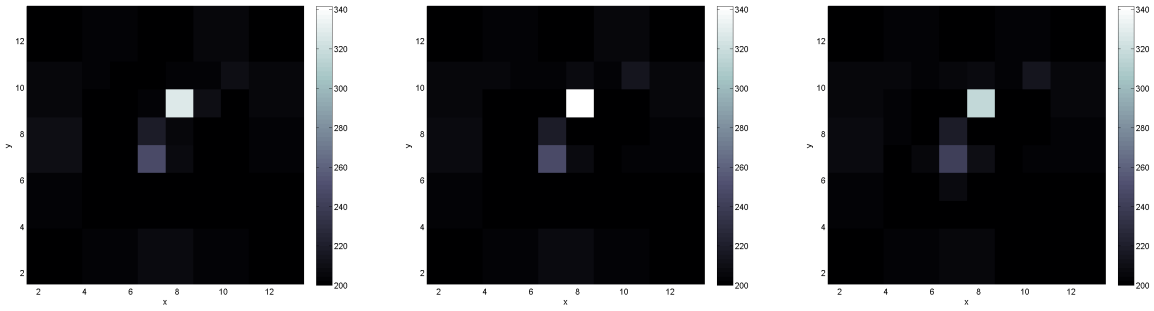

(a) Voxel Layer 1 (b) Voxel Layer 2 (c) Voxel Layer 3

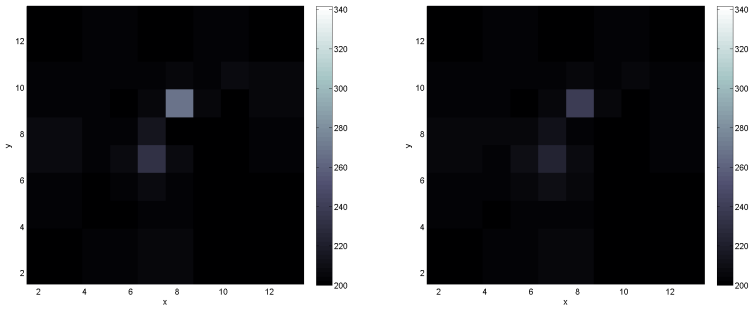

(d) Voxel Layer 4 (e) Voxel Layer 5

Figure 13. Conductivity reconstructions for two cylindrical objects, one of radius R_{25} and of conductivity 600mS/m, and the other of radius R_{15} and of conductivity 800mS/m, placed at positions $P5$ and $P6$, respectively, and $z = -3$mm.